



On the stress- and strain-based fatigue behavior of welded thick-walled nodular cast iron

Christoph Bleicher, Steffen Schoenborn, Heinz Kaufmann

Fraunhofer Institute for Structural Durability and System Reliability, Darmstadt, Germany

christoph.bleicher@lbf.fraunhofer.de, <https://orcid.org/0000-0002-0874-9548>

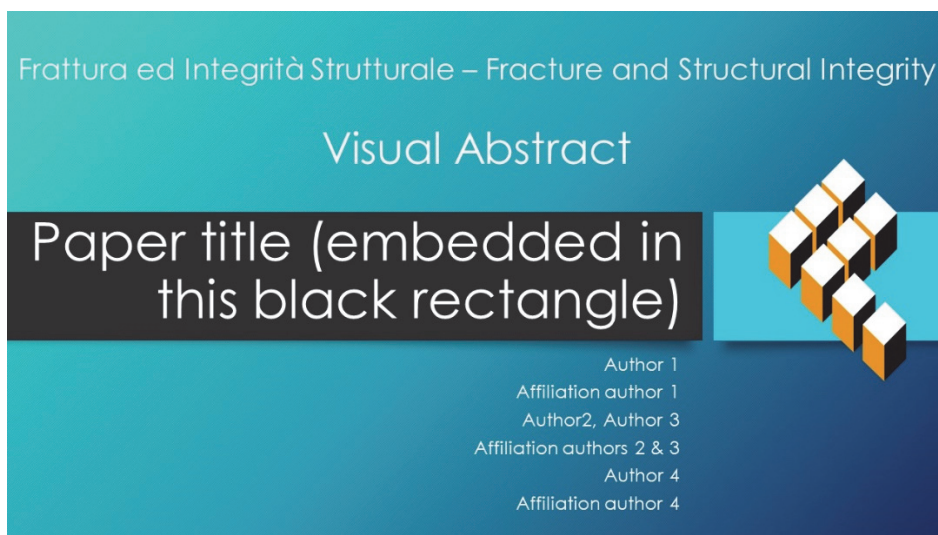
steffen.schoenborn@lbf.fraunhofer.de, <https://orcid.org/0000-0003-2743-1380>

heinz.kaufmann@lbf.fraunhofer.de, <http://orcid.org/0009-0002-6295-4363>

Masoud Alizadeh-Sh

Department of Wind and Energy Systems, Technical University of Denmark, 4000 Roskilde, Denmark

maaliz@dtu.dk, <http://orcid.org/0000-0001-9621-4991>



Citation: Bleicher, C., Schoenborn, S., Kaufmann, H., Alizadeh-Sh, M., On the stress- and strain-based fatigue behavior of welded thick-walled nodular cast iron, *Frattura ed Integrità Strutturale*, 68 (2024) 371-389.

Received: 31.01.2024

Accepted: 09.03.2024

Published: 15.03.2024

Issue: 04.2024

Copyright: © 2024 This is an open access article under the terms of the CC-BY 4.0, which permits unrestricted use, distribution, and reproduction in any medium, provided the original author and source are credited.

KEYWORDS. Fatigue, Nodular cast iron, Thick-walled, Welding.

INTRODUCTION

Cast components made of nodular cast iron (GJS) [1] are widely used in heavy industry and wind energy turbines, these components usually exhibiting wall thicknesses of 100 mm. Due to its wide range of material properties, with high strength and ductility, and the degree of freedom in design, GJS is used for highly loaded components such as rotor hubs, machine carriers, gear boxes and torque arms, sometimes exceeding 30 tons in weight. For those components



with high requirements, especially in terms of fatigue strength and stiffness, it is crucial to achieve a more or less perfect microstructure, especially in the highly loaded areas.

With increasing wall thickness of cast components, the likelihood of the occurrence of local material defects, such as pores, shrinkages and dross, also increases. Thus, these GJS components are usually not completely free of local material defects. In most cases, this leads to the rejection of the components, due to a lack of acceptance by the casting user and the certification bodies, since the effects on lifetime arising from the defects are not exactly known. In the case where material defects occur locally and near the component's surface, this causes a reduction of the component's lifetime, especially when sharp notches or stress gradients locally increase the stresses interfering with the defects. One measure to bring the components into usage for foundries is to determine the defect characteristics and remove the defect by a defined manufacturing and subsequent welding process. Nevertheless, repair welding is not accepted by certification bodies, due to a lack of knowledge of the cyclic material behavior of repair-welded nodular cast iron in wind energy applications. In the context of repair welding for wind turbines, DNV guidelines [2] require a special qualification of the welding company as well as a tested welding procedure approval (WPA or welding process specification WPS) and a registered test report (welding procedure approval record - WPAR) [2]. According to DNV [2], dissimilar welding is not permitted for cyclically stressed components, this being related to a lack of knowledge of the effect of repair welding on the local fatigue strength of the weld.

Within the research project »nodularWELD« [3], the possibilities for welding thick-walled nodular cast iron are investigated on ferritic (EN-GJS-400-18LT), ferritic silicon solid-solution strengthened (EN-GJS-450-18) and pearlitic (EN-GJS-700-2) cast iron grades, based on cast blocks with a wall thickness of 200 mm. In addition to the cast blocks, a wind energy turbine's hub made of EN-GJS-400-18LT was also made available for the present investigations. On all blocks and the hub weldings strain- as well as stress-based material investigations were conducted to assess the lifetime of a repair-welded component. During the welding experiments, different welding fillers were tested to achieve an optimum result, which turned out to be achieved by a dissimilar welding filler in a cold welding process. Afterwards, all three materials and material states were extensively investigated by strain- and stress-controlled fatigue tests under alternating loading, $R_e = -1$, $R_o = -1$, as well as tensile loading, $R_o = 0$. For this purpose, axial and bending specimens were removed from the cast blocks in the base material, the welding filler and the heat-affected zone. Additionally, the integral material state, comprising the base material, the heat-affected zone and the welding filler, was investigated. The bending specimens were used to show the influence of stress gradients on the materials with welds. Based on additionally performed metallographic and fractographic investigations, a comprehensive conclusion regarding the usability of welded cast components is drawn for practical application.

The present paper is based on the results derived from project »nodularWELD« [3]. Besides a summary of the findings discussed in [4], [5], [6] and [7] concerning the stress- and strain-based material behavior of EN-GJS-400-18LT and EN-GJS-450-18 with and without welds the present work compares the stress- and strain-based material behavior of pearlitic EN-GJS-700-2 with those of the ferritic EN-GJS-400-18LT and EN-GJS-450-18 grades. Moreover, a detailed insight into the microstructure and fracture surfaces of the three materials in the welded condition is provided. This paper summarizes all results of project »nodularWELD« [3] that have not been published to date.

STATE-OF-THE-ART

Welding of thick-walled wind energy components made of nodular cast iron is not permitted by certification bodies such as DNV. In the DNV guideline for the certification of wind turbines [2], repair welds are not accepted for cyclically loaded components. The quality of the cast components required according to [2], the mechanical properties and microstructure need to be verified on the basis of test specimens representative of the component both for the initial condition and for the condition post-processed by welding.

The DVS [8] proposes a fracture mechanical approach for welded components taking into account the base material, the welding filler metal and the heat-affected zone with different material properties and their effect on the static [9] and cyclic crack initiation behavior as well as the different crack propagation behavior. Verification methods for general application are currently only partially standardized, such as in the case of the fracture mechanics analysis as discussed in [10]. Unfortunately, the discussed approaches and methods are not accepted for wind energy application.

International Nickel [11] conducted a series of static and dynamic mechanical tests on welded joints of nodular cast iron. The mechanical properties of butt welds on ductile cast iron, gas and arc welded, using nickel-iron electrodes were reported [11]. Moreover, the property values of gas welds with a 5 % nickel filler rod (welding with filler metal of the same type) of butt welds on pearlitic GJS are given as a function of the component thickness of the casting.



Schock [12] summarizes investigations on the properties of welded joints with similar welding filler metal for the ferritic GJS grades EN-GJS-350-22 and EN-GJS-400-18. The cold welding was done electrically by using steel electrodes. The obtained quasi-static strength properties (tensile strength, yield strength, elongation at fracture) of such welds are even better than those of the base metal. Nevertheless, the fatigue strengths were determined to be comparable to those of the base materials. However, no dissimilar welds were taken into account. Further investigations were carried out by Schramm [13] with the aim of determining a database for grey cast iron and GJS materials.

Holdstock and Alizadehshamsabadi [14] report on their investigations of welds on nodular cast iron for large wind energy components. Especially in relation to the solid-solution strengthened EN-GJS-500-14, they showed that large cracks occur during the welding process and ledeburite occurs in the fusion line. Cracks even propagated into the base material due to high tensile stresses.

Bleicher et al. reported, in several contributions, parts of the results derived in the “nodularWELD” project [3 – 7]. Starting with [4], the stress- and strain-based cyclic material behavior for axial loading of EN-GJS-400-18LT was discussed in detail, as derived for the cast blocks. Based on investigations on axial specimens removed from the base material, the heat-affected zone, the welding filler and the integral material state comprising all three zones, it was shown that, especially for high elasto-plastic strains, the welding filler material itself shows the highest fatigue strength and the highest cyclic stress-strain curves compared to all investigated material states. For higher cycles and thus lower total strain amplitudes, the fatigue strengths for all investigated material states reach a comparable level. It was shown that the fatigue properties of the heat-affected zone and the base material are comparable. Thus, it seems that the area near the welding filler in the base material is quite unaffected by the welding process and the induced heat. On a stress-based view, defects in the welding filler material significantly decreased the fatigue strength and increased scatter bands compared to the base material. In this case, a lower Young’s modulus in the welding filler, arising from defects, needs to be taken into account during numerical simulation.

In [5 and 6], a comparison between the cyclic material behavior of welded EN-GJS-400-18LT and EN-GJS-450-18 is drawn, based on stress- and strain-based data for axial specimens removed from cast blocks for alternating loading, $R_e = -1$ and $R_o = -1$, as well as tensile loading, $R_o = 0$. In addition to axial specimens, bending specimens were also investigated in which the local material gradient coming from the welding is superimposed with a stress gradient. In relation to EN-GJS-400-18LT, the high silicon EN-GJS-450-18 was much more complicated to weld. In the following, the fatigue strength of the welded material showed a much lower fatigue strength than EN-GJS-450-18, both for axial and bending specimens. Additionally, axial fatigue investigations were conducted on a segment of a welded wind energy turbine made of EN-GJS-400-18LT. In relation to the material and welded condition removed from the cast blocks, an approximately 30 % higher fatigue strength could be determined for the specimens taken from the weld in the component. Those results were supplemented by stress-controlled fatigue data gathered in [6] for EN-GJS-700-2 under axial loading. For this GJS grade, only fatigue tests under axial loading could be conducted, but not for bending loading. For the welded bending specimens, large cracks in the heat affected zone occurred, preventing a successful fatigue test. Nevertheless, for axial loading, the welded EN-GJS-700-2 material showed the best fatigue strength under alternating and tensile loading in relation to the previously mentioned investigations on EN-GJS-400-18LT and EN-GJS-450-18.

The present paper aims to summarize the overall outcome of the project “nodularWELD” for which the work presented in [4 – 7] are fundamental and, moreover, discuss strain-based investigations on EN-GJS-700-2 on axial specimens as well as findings in relations to fractographic and metallographic investigations.

INVESTIGATED MATERIALS AND SPECIMEN REMOVAL

As already reported in [4 – 7], all materials were cast in blocks with 1000 mm x 600 mm with a thickness of 200 mm to account for wall thicknesses and local microstructures typical of real cast components. All three materials, EN-GJS-400-18LT, EN-GJS-450-18 and EN-GJS-700-2, have been investigated under stress- and strain-controlled fatigue tests on blocks, Fig. 1. Additional material of EN-GJS-400-18LT came from a hub of a wind energy turbine from serial production, as reported in [7], Fig. 1. The chemical compositions of all three materials cast in blocks in sound condition are given in Tab. 1. While the silicon content was elevated by about 1 % to achieve a solid-solution strengthening effect for EN-GJS-450-18, a higher copper content was used to provoke a pearlitic microstructure in EN-GJS-700-2.

After the casting process, all cast blocks and the component were inspected by non-destructive testing to ensure a macroscopic defect-free material situation. After non-destructive testing of the cast blocks and the hub using ultrasonic inspection, the hub was disassembled and grooves in a V-shape were milled into a section of the hub and into the cast blocks. These simulate the mechanically removed discontinuity area on a later serial component, which must be welded.

The groove was defined in terms of shape (V-shape), notch radius of the flanks (5 mm) and its depth (60 mm) in consultation with the project participants and with DNV in order to represent as realistic an application as possible, Fig. 1.

EN-GJS-400-18LT – cast block							
C	Si	Mn	Cr	S	Ni	Mg	Cu
3.72	1.97	0.20	0.03	0.01	0.01	0.044	0.02
EN-GJS-450-18 – cast block							
C	Si	Mn	Cr	S	Ni	Mg	Cu
3.36	2.93	0.20	0.03	0.01	0.02	0.05	0.02
EN-GJS-700-2 – cast block							
C	Si	Mn	Cr	S	Ni	Mg	Cu
3.66	1.89	0.40	n. d.	0.01	n. d.	0.05	1.06

n. d. – not determined

Table 1: Chemical compositions (wt%; Fe bal.) of the investigated materials in addition to results given in [6]

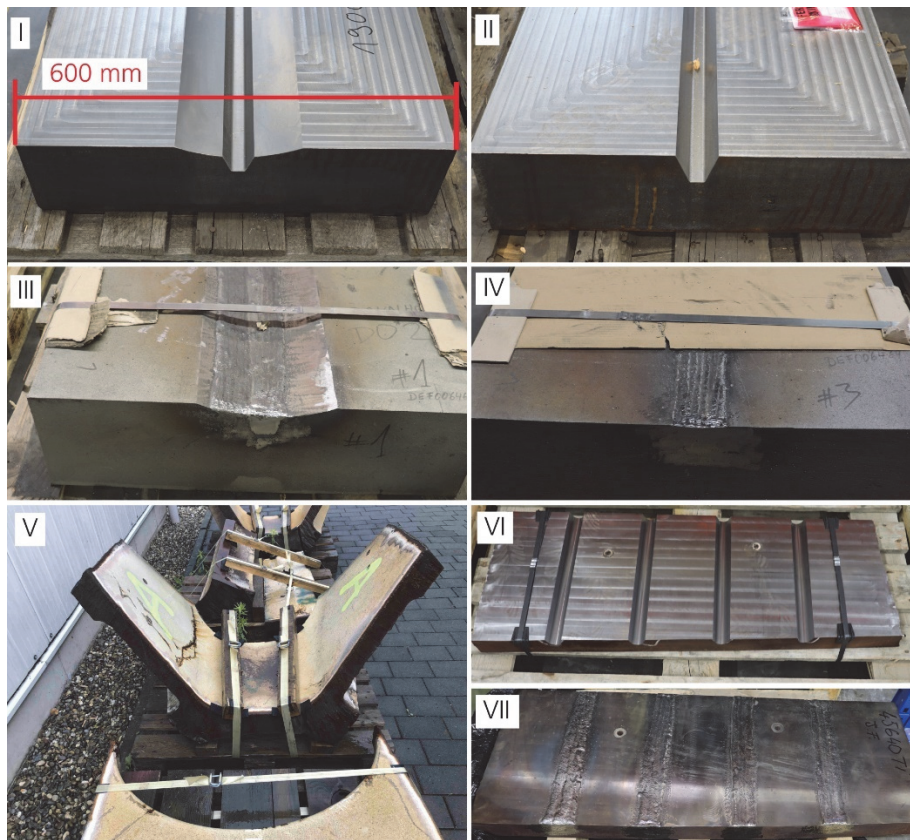


Figure 1: I: cast block with groove for removal of bending specimens; II: cast block with groove for removal of axial specimens; III + IV: cast blocks with welded grooves; V: cut hub into smaller segment; VI: hub's segment with grooves; VII: hub's segment with welded grooves.

Subsequently, preliminary welding tests were carried out on small sections of the cast blocks to demonstrate the basic applicability of the welding filler on the basis of static characteristic values [3]. Cold and hot welding was performed with both dissimilar and similar filler metals in different configurations summarized in Tab. 2. The welding of the GJS materials was based on the following considerations: Since the welding process needs to be conducted easily and despite the location and even in a maintenance procedure on-site, manual electrode welding was the method to choose. Moreover, the aim was to produce the welding as close as possible to a realistic environment and not one conducted in the laboratory. This, in turn, had the advantage of being able to apply the results over a wide range of components and applications, but entailed the necessity of having to accept minor flaws in the weld seam. Accepting those flaws is possible when the removed casting defect has a significantly larger extent (> 10 mm) compared to the welding pores that might occur.

The weldings were conducted on the basis of a continuous wire process under gas shield with 100 % Ar with regard to EN ISO 4063 [15] at a temperature of 130 °C, a current of 150 to 160 A, voltage of 20 - 25 V and a wire speed of 4 – 6 m per minute. Also, an intermediate layer hammering was applied. The welding filler used and the results of the preliminary tests for each GJS material are shown in Tab. 2.

Thus, the cast blocks and the component made of EN-GJS-400-18LT and EN-GJS-700-2 were subsequently cold welded with the filler metal CastoMag 45640 Ti (Ni-Fe-Mn-Ti alloy) and the cast plates made of EN-GJS-450-18 with EnDoTec Do 23 (Ni-Fe-Mn alloy). EN-GJS-450-18 showed a tendency to crack during the welding procedure. This behavior is also described by investigations in [14] on EN-GJS-500-14, which is also a ferritic GJS grade with a high silicon content.

This has the additional advantage for the subsequent application that local preheating by several 100 K can be omitted. The filler metals used hot, on the other hand, showed strong influences on the local microstructure of the base materials, high scattering and, in some cases, low quasi-static properties. Tab. 2 shows a list of all the tests carried out according to the different filler metals. Based on the results of the preliminary welding investigations, the cast blocks and the component segments were welded with the corresponding welding filler.

Welding filler	Material		
	EN-GJS-400-18LT	EN-GJS-450-18	EN-GJS-700-2
Hot welded			
Castolin 2-26D	not investigated	unsuitable	not investigated
Teromatec 4226	not investigated	unsuitable	not investigated
ENDOTec DO* 636*	unsuitable	unsuitable	not investigated
Cold welded			
Castolin 2-44	unsuitable	not investigated	unsuitable
Castolin XHD 2230	unsuitable	unsuitable	unsuitable
CastoMag 45640 Ti	suitable	unsuitable	suitable
EnDoTec Do 23	unsuitable	suitable	unsuitable

Table 2: Investigated welding filler for each GJS grade.

For the fatigue tests, different specimen geometries, depicted in Fig. 2, were used. Axial specimens with gauge diameters d of 6 and 9 mm and bending specimens (40 mm x 70 mm and (25 mm x 25 mm) were machined from the cast blocks and the hub segments. The axial specimens with diameter $d = 6$ mm were taken from the base material, the welding filler and the heat-affected zone to investigate in detail the effect of the welding process on the local cyclic material behavior. For a direct comparison of the material strength, so-called “integral” axial fatigue specimens with a diameter $d = 9$ mm were machined across all the zones, which are the base material, the heat-affected zone and the welding filler. Additionally, bending specimens (IV and V, Fig. 2) were removed from additional cast blocks and the component to determine the fatigue behavior of the integral material state in combination with a superimposed stress gradient, as might occur in large cast wind energy components. The bending specimens were chosen to be comparably large in order to achieve a small stress gradient in the specimens, typical for large components.

After the manufacturing process, all axial specimens including welding filler were analyzed by non-destructive testing based on X-rays. This process revealed pores in the welding filler material due to the welding process in sizes up to a few millimeters, Fig. 3. Nevertheless, all specimens were used for the fatigue tests to assess the range of scatter bands. This helps to understand the worst case scenarios of welding large GJS components and the profit or loss due to welding in comparison to the base material with defects from the casting process.

CYCLIC MATERIAL INVESTIGATIONS

All fatigue investigations were conducted until a crack initiated or until the limit number of cycles of $N_{lim} = 1 \cdot 10^7$ at room temperature and in ambient air. While the strain-controlled fatigue tests were conducted only for alternating loading, $R_\epsilon = -1$, the stress-controlled fatigue tests were performed both under alternating, $R_\sigma = -1$, and tensile loading, $R_\sigma = 0$, to assess the influence of mean stresses and to derive numbers for the mean stress sensitivity M , according to [16].

The strain-controlled fatigue tests were performed on servo-hydraulic test rigs with maximum loads of 63 kN under constant amplitude loading to derive information about the cyclic, elasto-plastic behavior of the base material, the welding filler and

the heat-affected zone according to SEP1240 [17]. [17] provides guidelines for the determination of cyclic material parameters with reference to specimen types, test boundary conditions, calibration standards for the test equipment and final evaluation of the results. To determine the elasto-plastic material behavior for higher total strains, $\epsilon_{a,t}$, lower test frequencies are necessary to enable a material relaxation. In this research project, the investigations were conducted with a test frequency of $f = 0.1$ to 25.0 Hz, according to [17].

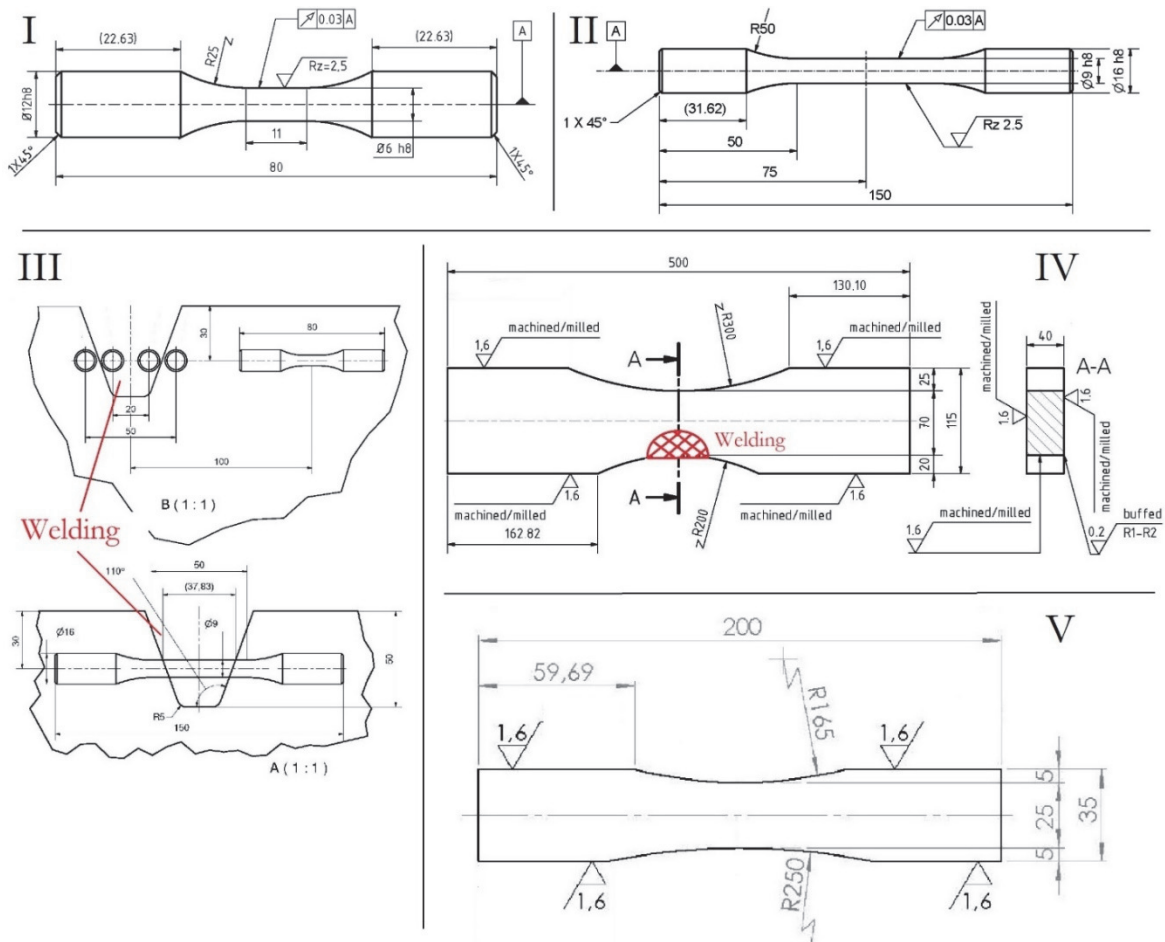


Figure 2: I: axial fatigue specimens used for strain-controlled fatigue tests with $K_t = 1.04$; I: axial fatigue specimens used for strain- and stress-controlled fatigue tests with $K_t = 1.00$ comprising the welding filler, the heat affected zone and the base material called “integral material state”; III: removal position for the axial specimens in the welding filler, the heat affected zone and the base material; IV: bending specimen removed from the cast blocks; V: bending specimen removed from the component.

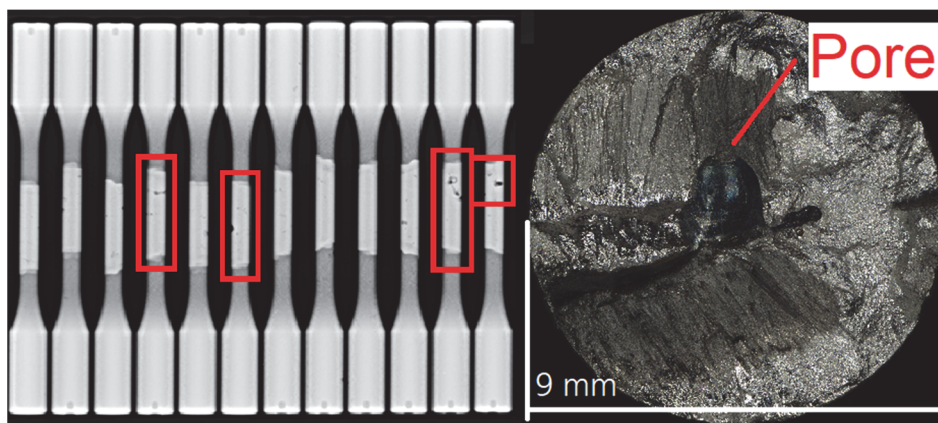


Figure 3: Left: X-ray film with specimens removed from the integral material state with pores; right: cross section of a failed specimens with a pore in the welding filler.



The resulting test data were evaluated by calculating the cyclic stress-strain curves according to Ramberg and Osgood [18] and following the strain-life curves according to Coffin [19], Manson [20], Basquin [21] and Morrow [22]. For the calculation of the strain-life and the cyclic stress-strain curve parameters according to SEP1240 [17], the elastic strain $\epsilon_{a,e}$ is first calculated by dividing the stress amplitude σ_a by the Young's modulus E. The Young's modulus E is determined from the strain-controlled tests for each material. To derive the plastic fraction of the total strain, the calculated elastic strain $\epsilon_{a,e}$ is subtracted from the measured total strain $\epsilon_{a,t}$.

By plotting and applying linear regression through the elastic and plastic fractions of each strain-controlled fatigue test, one is able to calculate the strain-life curve parameters. These are the parameters ϵ_f (fatigue ductility coefficient), σ_f (fatigue strength coefficient), b (fatigue strength exponent) and c (fatigue ductility exponent). For the calculation of the cyclic stress-strain curve parameters according to Ramberg and Osgood [18], the compatibility, defined for instance in [23], can be used. The stress-controlled fatigue tests on axial and bending specimens were conducted on electric resonance test rigs with maximum loads of 100 kN and 200 kN, respectively. The statistical evaluation to derive the parameter of the SN curve followed the maximum likelihood method according to Spindel and Haibach [24] and Stoerzel [25] for a probability of survival of $P_S = 10\%$, 50% and 90% . Furthermore, the scatter band T_σ and the slope of the SN curve k was determined. The slope after the knee point N_k k^* was assumed to be 44.9, which corresponds to a decrease in fatigue strength of 5 % per decade, according to [26], which is in good agreement with the investigation of [27] on other nodular cast iron materials.

	EN-GJS-400-18LT	EN-GJS-450-18	EN-GJS-700-2
Removal position	Base material		
Fatigue strength coefficient σ'_f [MPa]	567.4	703.7	793.6
Fatigue strength exponent b [-]	-0.0865	-0.0895	-0.1007
Fatigue ductility coefficient ϵ'_f [m/m]	0.2532	0.1282	0.0936
Fatigue ductility exponent c [-]	-0.7353	-0.6549	-0.6000
Cyclic yield strength $R'_{p0,2}$ [MPa]	316.0	403.5	316.0
Cyclic hardening coefficient K' [MPa]	621.45	625.3	767.1
Cyclic hardening exponent n' [-]	0.1089	0.0705	0.0998
Young's modulus E [GPa]	164.0	168.1	167.1
Removal position	Heat affected zone		
Fatigue strength coefficient σ'_f [MPa]	570.5	750.5	938.8
Fatigue strength exponent b [-]	-0.08355	-0.0950	-0.1090
Fatigue ductility coefficient ϵ'_f [m/m]	0.1046	0.9515	0.1253
Fatigue ductility exponent c [-]	-0.6067	-0.9441	-0.6613
Cyclic yield strength $R'_{p0,2}$ [MPa]	327.1	399.1	489.3
Cyclic hardening coefficient K' [MPa]	468.5	716.0	1031.4
Cyclic hardening exponent n' [-]	0.0578	0.0940	0.1200
Young's modulus E [GPa]	163.0	167.3	167.0
Removal position	Welding filler		
Fatigue strength coefficient σ'_f [MPa]	1299.0	865.3	909.9
Fatigue strength exponent b [-]	-0.1405	-0.0987	-0.0895
Fatigue ductility coefficient ϵ'_f [m/m]	3.865	0.1150	0.1016
Fatigue ductility exponent c [-]	-0.9996	-0.5229	-0.5649
Cyclic yield strength $R'_{p0,2}$ [MPa]	419.6	405.6	490.8
Cyclic hardening coefficient K' [MPa]	823.0	856.3	1010.9
Cyclic hardening exponent n' [-]	0.1084	0.0799	0.1163
Young's modulus E [GPa]	142.0	147.3	146.0
Removal position	Integral material state		
Fatigue strength coefficient σ'_f [MPa]	597.0	-	1090.2
Fatigue strength exponent b [-]	-0.0954	-	-0.1480
Fatigue ductility coefficient ϵ'_f [m/m]	0.0249	-	0.0893
Fatigue ductility exponent c [-]	-0.5849	-	-0.7481
Cyclic yield strength $R'_{p0,2}$ [MPa]	374.9	-	476.3
Cyclic hardening coefficient K' [MPa]	656.3	-	915.8
Cyclic hardening exponent n' [-]	0.0901	-	0.1052
Young's modulus E [GPa]	161.0	-	158.7

Table 3: Cyclic material parameters for the cyclic stress-strain and the strain-life curves for all investigated material states and GJS grades.

STRAIN-BASED MATERIAL BEHAVIOR

Fig. 4 and Fig. 5 depict the cyclic stress-strain and the strain-life curves for the investigated EN-GJS-700-2 for the base material and the corresponding welding filler, integral material states and the heat-affected zone. All fatigue data, characterizing the cyclic stress-strain curves and the strain-life curves for all three materials, are summarized in Tab. 3.

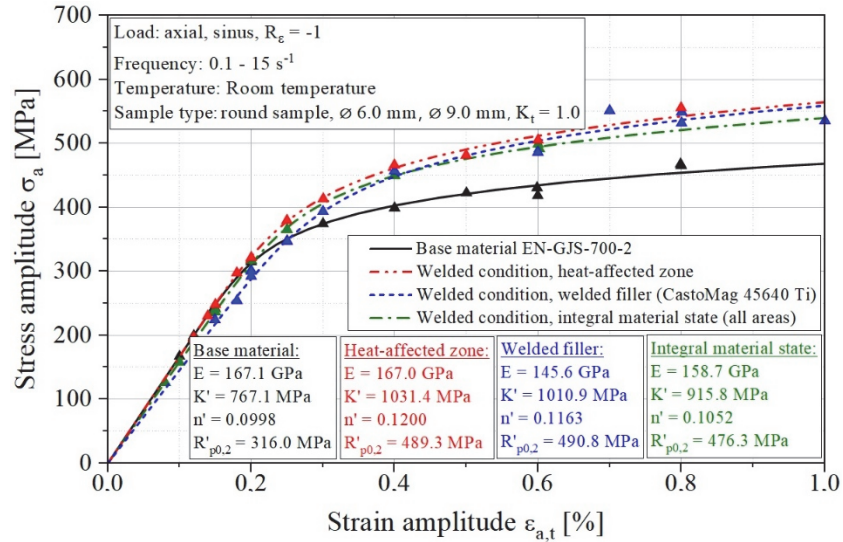


Figure 4: Cyclic stress-strain curves for the base material in comparison to those of the welding filler, the heat-affected zone and the integral material state for EN-GJS-700-2.

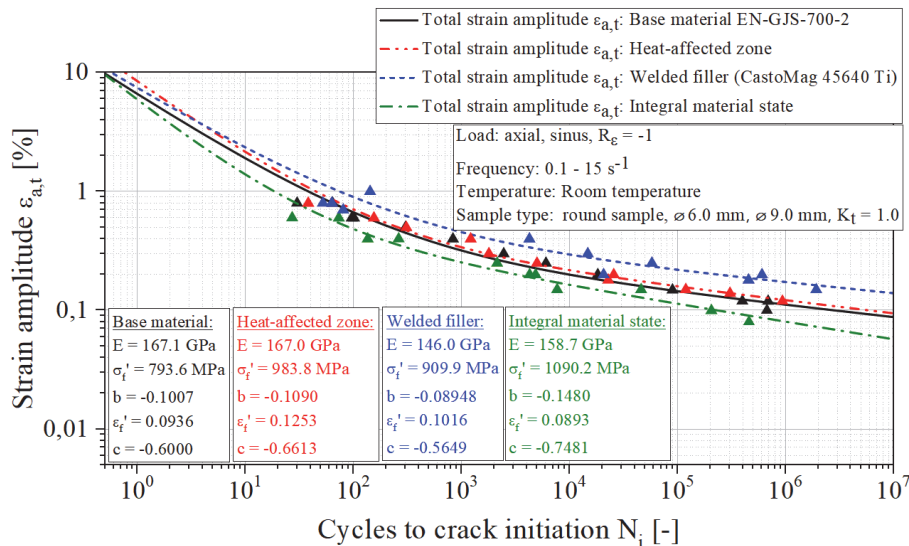


Figure 5: Strain-life curves for the base material in comparison to those of the welding filler, the heat-affected zone and the integral material state for EN-GJS-700-2.

In comparison to the results discussed in [6], the Young's modulus of the integral material state and the welding filler show drastically reduced values. Due to the occasionally occurring pores in the welding filler, the stiffness and thus the Young's modulus is reduced. Usually, the Young's modulus E of a sound material condition is well above 160 GPa, which is a typical value for thick-walled nodular cast iron, found in [28].

For EN-GJS-700-2, the curves for the heat-affected zone, the welding filler and the integral material state show comparable strength and much higher curves compared to the base material, Fig. 4. This is unlike EN-GJS-450-18 and EN-GJS-400-18LT, for which the cyclic stress-strain curves for the heat-affected zone and the base material are, over a wide range, more or less identical. Nevertheless, the cyclic stress-strain curves for the base material for EN-GJS-450-18 and EN-GJS-700-2

are also identical. This is a result of a strong cyclic hardening effect of the EN-GJS-450-18 base material, while EN-GJS-700-2 has the tendency to a cyclic softening effect [27].

Looking at the strain-life curves for all materials, the welding filler shows the highest fatigue strength in relation to the base material and the heat-affected zone as well as the integral material state. In comparison to the other materials reported in [6], the integral material state reaches the lowest fatigue strength.

All strain-based fatigue data can be used for a strain-based fatigue assessment approach. This enables a numerical component simulation of a thick-walled component with a repair weld by assigning the different Young's moduli, as well as the quasi-static and cyclic strain life curves, to the different regions of base material, heat-affected zone and welding filler. This enables a local resolution of the material behavior for a detailed lifetime assessment of a welded component.

STRESS-BASED MATERIAL BEHAVIOUR

Exemplarily the determined fatigue results are summarized in Fig. 6, Fig. 7 and Fig. 8 as well as in Tab. 4 in the form of the SN curve parameters and the mean stress sensitivity M [16] for the axial fatigue specimens removed from the base material and for the integral material state for the pearlitic EN-GJS-700-2 (Fig. 6) as well as a comparison of the results for the axial and bending specimens for all materials (Fig. 7 and Fig. 8).

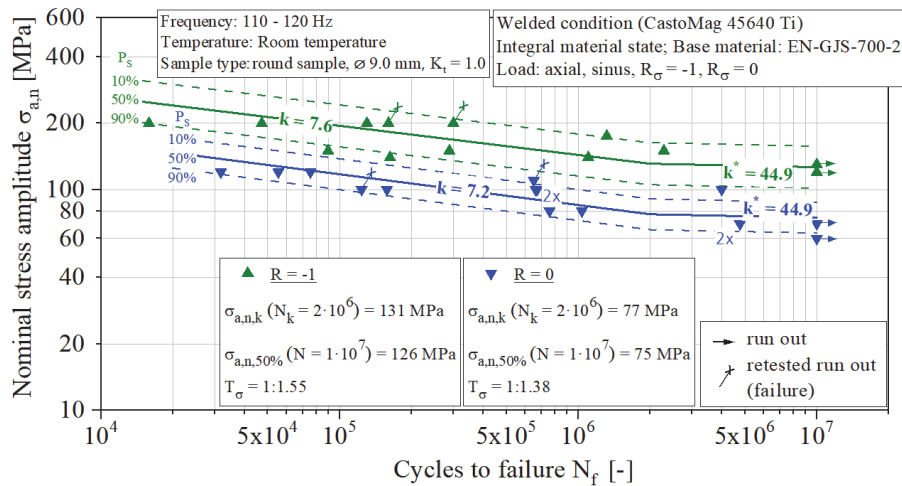


Figure 6: Stress-life curves for the integral material state for EN-GJS-700-2.

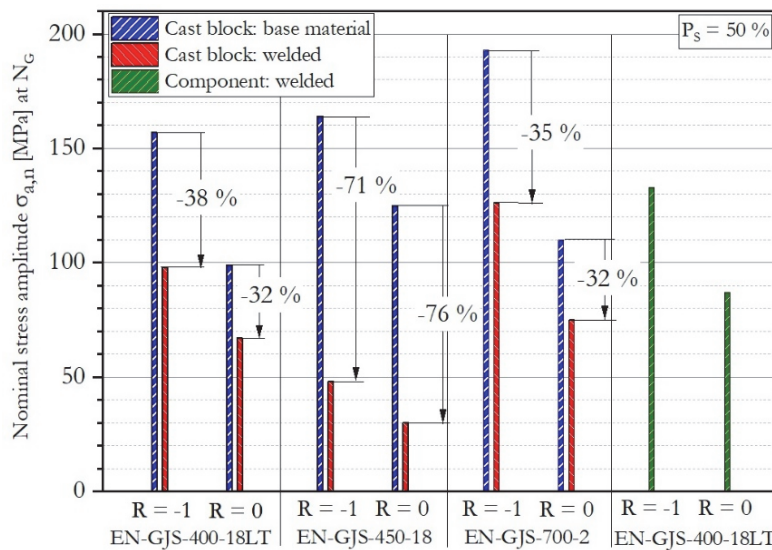


Figure 7: Summary of the fatigue strength determined on the axial specimens under stress control with and without welding.

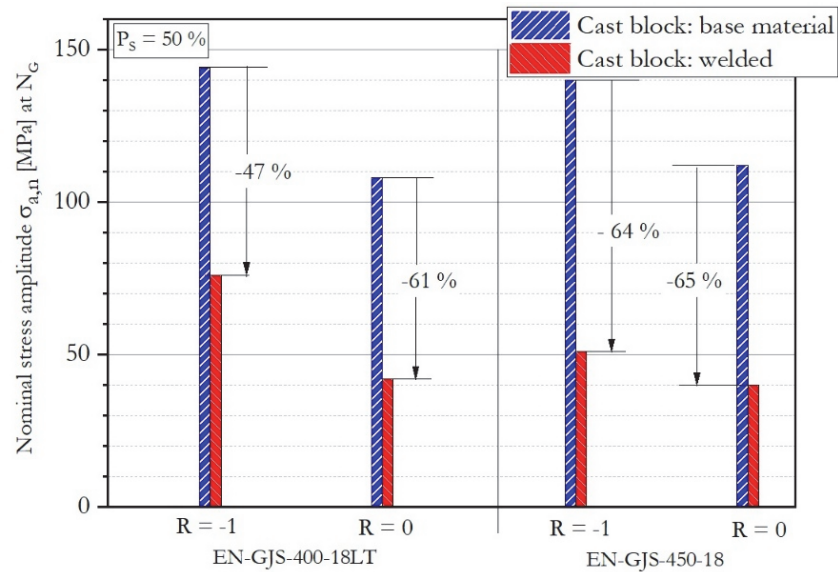


Figure 8: Summary of the fatigue strength determined on the bending specimens under stress control with and without welding.

For EN-GJS-700-2, it was not possible to determine fatigue results for the welded bending specimens since, after manufacturing the specimens from the blocks, large cracks were present in one side of each bending specimen in the fusion line, making a fatigue investigation valueless. Such defects did not occur in all of the other batches, so it seems that, for this specific cast block, the welding procedure was not conducted properly.

Looking at the results for the base material, not surprisingly and in good agreement with the investigations of [27], [28] and [29], EN-GJS-400-18LT shows the lowest fatigue strength followed by EN-GJS-450-18 and EN-GJS-700-2, both for axial and bending loading and for both load ratios, with one exception: the investigated EN-GJS-700-2 shows a very high mean stress sensitivity of $M = 0.75$ due to a comparably low nominal stress amplitude for tensile loading, $R_\sigma = 0$, $\sigma_{a,Nlim} = 110$ MPa, this being 15 MPa lower than the corresponding value for EN-GJS-450-18.

For the welded condition, it was not possible to determine a knee point during the statistical evaluation in all cases. For EN-GJS-400-18LT ($R_\sigma = 0$) and EN-GJS-450-18 ($R_\sigma = -1$ and $R_\sigma = 0$), the bending specimens in the welded condition showed no knee point until N_{lim} and, thus, a behavior similar to that under corrosive media.

The integral material state, taken from the rotor hub segment, achieved a relatively high fatigue strength with nominal stress amplitudes of $\sigma_{a,n} = 133$ MPa for $R_\sigma = -1$ and $\sigma_{a,n} = 87$ MPa for $R_\sigma = 0$ at $1 \cdot 10^7$ cycles, particularly in comparison to EN-GJS-400-18LT made from cast blocks. These even exceed the characteristic values determined for EN-GJS-700-2, which may also be due to the lower thickness of the weld and the associated lower probability of pores occurring. In this respect, the characteristic values of welded cast blocks compared in this study should be considered to be conservative if they are used to evaluate the local strength of a weld in GJS.

For all welded material states, a drop in fatigue strength was determined both for axial and bending specimens. An overview and comparison for all derived nominal stress amplitudes is given in Fig. 7 and Fig. 8 for axial and bending specimens, respectively. It turns out that the highest loss in fatigue strength is present for EN-GJS-450-18. The reduction in the nominal stress amplitude, both for $R_\sigma = -1$ and $R_\sigma = 0$, is so high that EN-GJS-450-18 cannot benefit from the higher fatigue strength of the base material in comparison to EN-GJS-400-18LT. In the worst case, a reduction of 76 % needs to be taken into account for EN-GJS-450-18, when being welded with EnDoTec Do 23. Nevertheless, it is worth mentioning that the highest reduction occurred on the integral axial specimens, while, for bending load, EN-GJS-400-18LT also showed high losses in fatigue strength. The best results were derived for EN-GJS-700-2 under axial loading. Although the relative reduction in fatigue strength is the same as for EN-GJS-400-18LT, the much higher strength of the base material leads to fairly good nominal stress amplitudes in the welded condition, Fig. 7.

The mean-stress sensitivities M for each base material condition investigated do not show a uniform trend. For example, there is no fundamental increase in mean-stress sensitivity with tensile strength. While for EN-GJS-400-18LT reaches $M = 0.58$ under axial load, the EN-GJS-450-18 only achieves a value of $M = 0.31$. The mean stress sensitivity then increases again to a very high value of $M = 0.75$ for the EN-GJS-700-2. Under bending, the mean stress sensitivity for the base material decreases to $M = 0.33$ for EN-GJS-400-18LT and $M = 0.25$ for EN-GJS-450-18, which may be related to a change in the highly stressed volume of the specimens or to the local change in stress-strain behavior. Studies by [30] on thick-walled GJS also showed a similar dependence. As a comparison, the DNV guideline [2] provides values for the mean stress

sensitivity as a function of the standardized tensile strength. For EN-GJS-400-18LT DNV [2] calculates a values of $M_{400} = 0.22$, while for EN-GJS-450-18 and EN-GJS-700-2 values of $M_{450} = 0.24$ and $M_{700} = 0.33$ are determined. FKM guideline [31] assumes a constant value of $M = 0.4$ for all GJS materials instead.

Material	Removal position	Sample geometry	Material state	Number of specimens investigated	Load ratio R_σ	Slope k [-]	Knee point N_k ($\cdot 10^5$) [-]	Nominal stress amplitude $\sigma_{a,Nlim}$ at N_{lim} [MPa]	Scatter band T_σ [-]	
EN-GJS-400-18LT	Cast block	Axial	Base material	12	-1	9.5	10	157	1:1.23	
				13	0	5.6	3	99	1:1.13	
			Mean stress sensitivity $M = 0.58$							
		Integral material state	13	-1	5.4	30	98	1:1.44		
			18	0	5.6	10	67	1:1.38		
			Mean stress sensitivity $M = 0.46$							
	Bending	Base material	10	-1	6.4	10	144	1:1.17		
			12	0	7.4	20	108	1:1.13		
			Mean stress sensitivity $M = 0.33$							
		Base, heat-affected zone and welding filler	12	-1	3.2	20	76	1:1.51		
			11	0	3.8	-	42	1:1.39		
			Mean stress sensitivity $M = 0.81$							
	Component	Axial	Integral material state	14	-1	5.1	6	133	1:1.22	
				6	0	5.8	6	87	1:1.23	
		Mean stress sensitivity $M = 0.53$								
		Bending	Base, heat-affected zone and welding filler	15	-1	3.5	3	99	1:1.39	
	EN-GJS-450-18	Cast block	Axial	Base material	17	-1	8.6	10	164	1:1.16
					17	0	14.7	20	125	1:1.20
Mean stress sensitivity $M = 0.31$										
Integral material state			11	-1	6.5	10	48	1:1.22		
			12	0	9.3	20	30	1:1.29		
Mean stress sensitivity $M = 0.60$										
Bending		Base material	10	-1	4.9	10	140	1:1.11		
			10	0	6.3	10	112	1:1.11		
			Mean stress sensitivity $M = 0.25$							
		Base, heat-affected zone and welding filler	13	-1	7.3	-	51	1:1.36		
	12		0	5.9	-	40	1:1.62			
Mean stress sensitivity $M = 0.28$										
EN-GJS-700-2	Cast block	Axial	Base material	16	-1	9.4	10	193	1:1.12	
				14	0	6.7	10	110	1:1.29	
			Mean stress sensitivity $M = 0.75$							
		Integral material state	11	-1	7.6	20	126	1:1.55		
			12	0	7.2	20	75	1:1.38		
		Mean stress sensitivity $M = 0.68$								

Table 4: Cyclic material parameters for the stress-life curve for all investigated material states and GJS grades.

For the integral material condition and the welded bending specimens, there is also no uniform behavior with regard to mean stress sensitivity. While M for the EN-GJS-400-18LT and the EN-GJS-700-2 drops slightly under axial load, a more than doubled value of $M = 0.81$ is achieved for the mean stress sensitivity under bending load (Tab. 4). For the EN-GJS-450-18, the effect is the opposite, so that a doubling of M is recorded under axial load and a slight reduction under bending load.



With regard to the resulting slope in the area of the fatigue strength, it can be seen that this becomes significantly steeper across almost all SN curves due to the local notch effect of the weld (Tab. 4). Only, in the case of EN-GJS-450-18, there is a significantly lower value for the base material with $k = 4.9$ under alternating load in contrast to the welded condition ($k = 7.3$) with the same load ratio.

The scatter bands determined for the base material are within the usual range for thick-walled GJS for all materials investigated, [27, 29, 30], of $1:1.11 < T_{\sigma} \leq 1:1.29$. For example, for EN-GJS-400-15 Bleicher [27] recommends for ferritic and pearlitic thick-walled GJS materials a scatter band of $T_{\sigma} = 1:1.30$ for component design.

In the welded condition, an increase in the scatter bands compared to those of the base material was generally recorded, which can be attributed both to the gradient in the material condition due to the welding, on the one hand, and to the welding pores present in some cases, on the other. Scatter bands in the range $1:1.22 < T_{\sigma} \leq 1:1.62$ were determined for the axial and bending specimens in the welded condition. As a result, the safety factors for the design of welded areas also increase. For a conservative approach to the design of corresponding welded areas, a scatter factor of $T_{\sigma} = 1:1.70$ should therefore be assumed. However, this means that the scatter band is still at a significantly lower level compared to those that would have to be used for the design of shrinkage affected areas in thick-walled GJS. According to Bleicher [28], a minimum scatter factor of $T_{\sigma} = 1:2.30$ is to be expected here.

METALLOGRAPHIC AND FRACTOGRAPHIC INVESTIGATIONS

In addition to the conducted fatigue investigations, metallographic and fractographic investigations were also carried out on axial and bending samples. Based on DIN 945 [32] for the cast blocks and the component, graphite analysis was conducted to determine graphite particle density, graphite size, graphite form and nodularity, (Tab. 5 and Fig. 9). Of particular note here is a smaller proportion of pearlite in the EN-GJS-400-18LT and a proportion of ferrite in the EN-GJS-700-2. The EN-GJS-450-18 has significantly smaller graphite nodules compared to the component and the other two materials. The nodularity index of the EN-GJS-400-18LT (43) is comparatively low, which is also due to the graphite nodules being very close together and touching each other in the structure, as well as many elongated graphite particles. The graphite spheres in contact with each other were deliberately not separated.

Material	EN-GJS-400-18LT		EN-GJS-450-18	EN-GJS-700-2
Removal position	Cast block	Component	Cast block	Cast block
Graphite particle density [1/mm ²]	65	58	75	57
Graphite form [%] (fraction V + VI)	62	95	90	91
Graphite size [%] (fraction 5 + 4)	74	92	65	71
Nodularity [-]	43	69	74	63

Table 5: Results of the metallographic investigations for the graphite in the base material for all GJS grades.

In addition to the microsections to characterize the base material, microsections and fracture surface images were also taken on samples with welds in order to better describe the weld metal, the heat transfer zone, local defects and the fracture behavior. Moreover, hardness maps of details covering the base material, the welding filler and the heat affected zone were conducted.

Tabs. 6, 7 and 8 show examples of micrographs, hardness maps and etched sections with detailed images differentiated by material. Smaller pores can be seen locally in the filler metal in all materials, as already expected from the radiographic results. Independent of the material is the local occurrence of cracks or delaminations in the transition area between the filler metal and the base material. They are caused by insufficient penetration welding or stresses due to the welding process. These microstructural delaminations are visible in all materials.

All materials show strong carbide formation and boundary layers of pearlite and harder phases, such as martensite and ledeburite, in the transition area between the filler metal and the base metal, which results in the local increase of the hardness. The hardness maps prove the formation of hard phases since hardness increases locally to up to 800 HV, while the base material and the welding filler usually reach 300 to 450 HV. Only the hardness map for EN-GJS-700-2 shows values up to 500 HV for the base material, which can be referred to the pearlitic matrix having a higher hardness compared to the ferritic matrix of EN-GJS-400-18LT and EN-GJS-450-18.

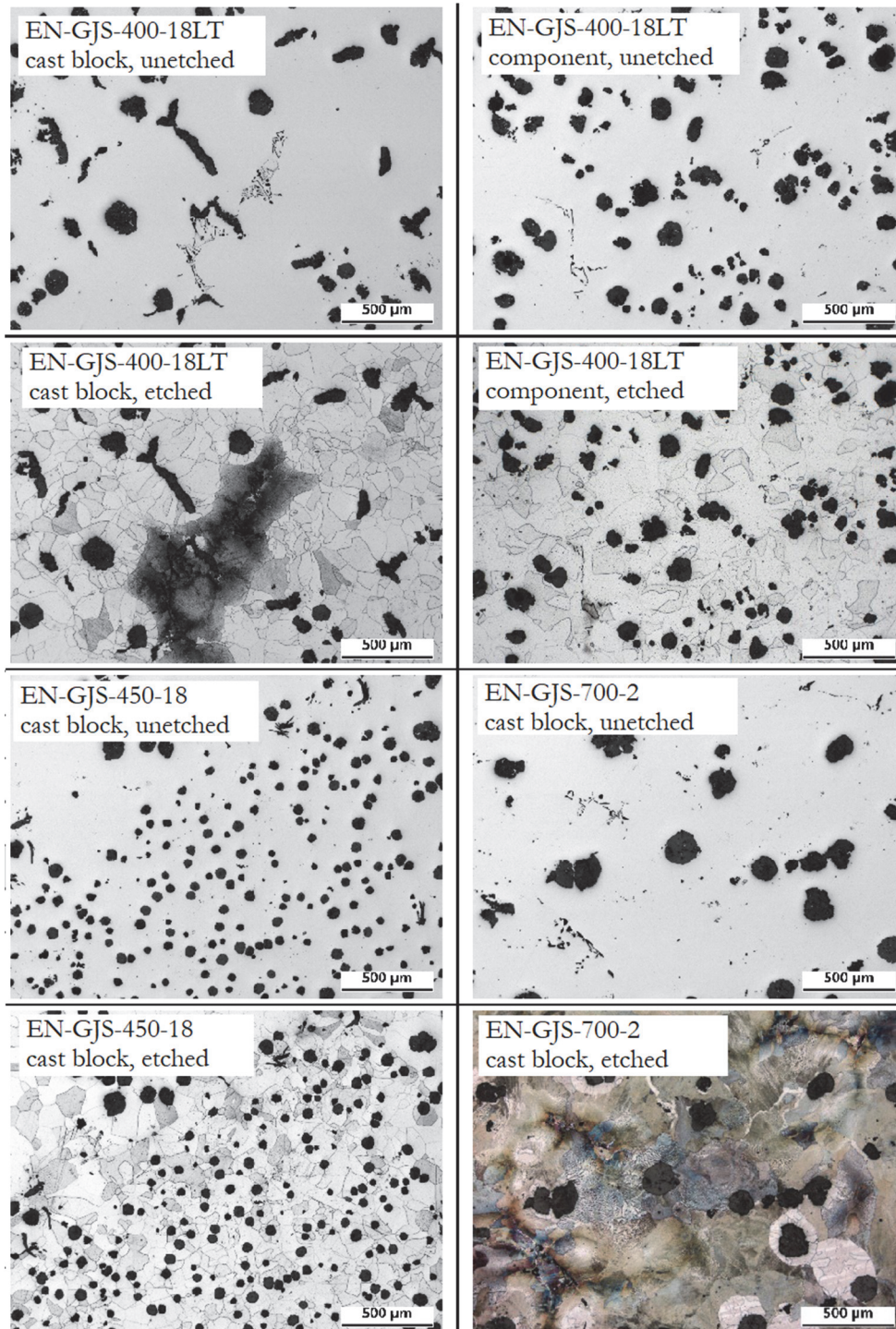


Figure 9: Examples for unetched and etched sections of all investigated materials.

Moreover, Tabs. 6, 7 and 8 provide some examples of fracture surfaces and detailed images. Regardless of the filler and base metals, most of the samples showed failure in the transition area between the filler metal and the base metal. However, there were also samples with failure in the weld filler material, which can be attributed to missing connections within the weld filler material or to delamination or even the occurrence of pores. In some cases, there were also crack-like structures in the weld filler material that favored failure, as shown in Tab. 8 on a sample of EN-GJS-450-18.

For the bending samples, the failure mostly started in the transition area between the filler metal and the base one and then continued through the base material, being no longer stopped there. In summary, the transition area can therefore be identified as the main starting point for the failure of the specimens.

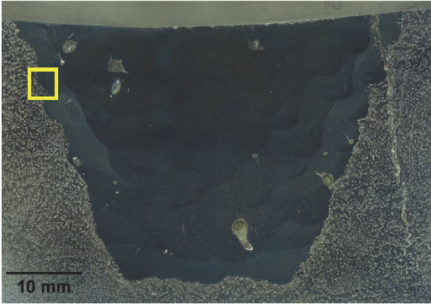
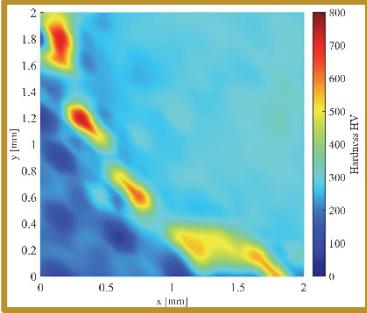
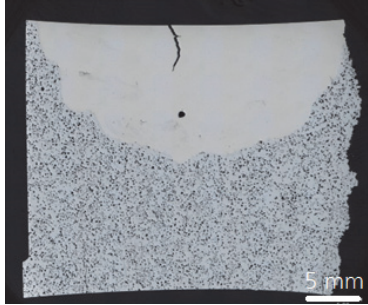
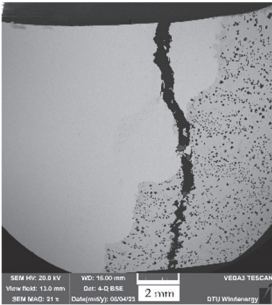
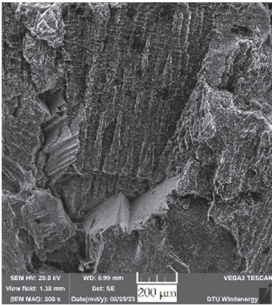
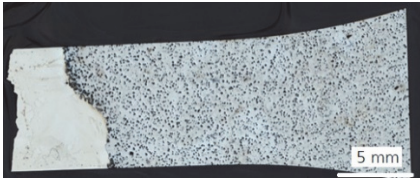
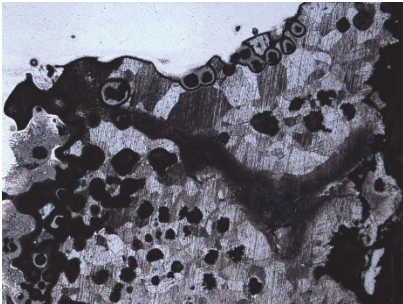
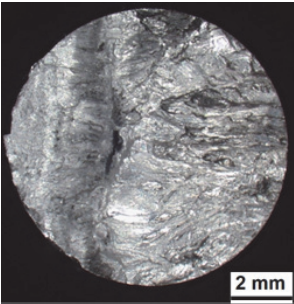
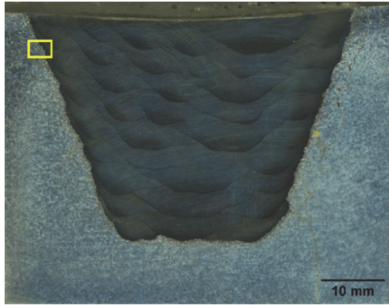
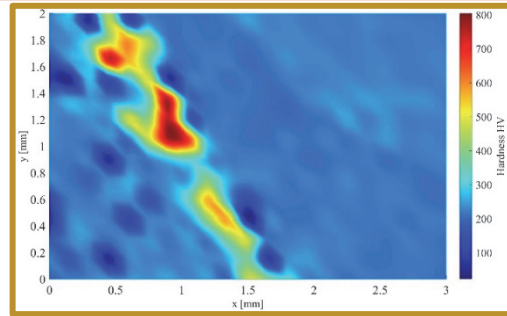
EN-GJS-400-18LT		
Cast block		Component
		
Macroscopic picture of the etched welding with local pores and a fatigue crack	Hardness map at the edge of the fusion zone	Etched section of the complete cross section of a bending specimen from the hub with small pores and a fatigue crack in the welding filler
		
Crack through welding filler and the base material	Solidification structure inside the fusion zone	Etched section of the complete cross section of an axial specimen from the hub
		
Etched section of the fusion line and the heat affected zone with hard martensitic and ledeburitic microstructures	Fracture surface of an axial specimen with failure in the welding filler	

Table 6: Examples of micrographs, hardness maps and etched sections for EN-GJS-400-18LT with welds

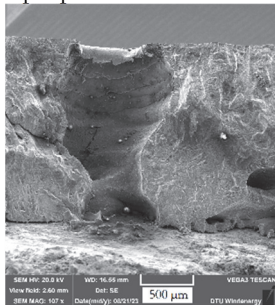
EN-GJS-450-18 cast block



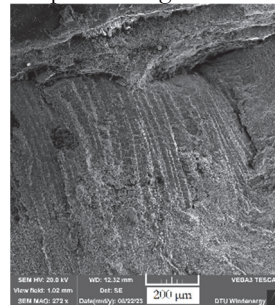
Macroscopic picture of the etched welding



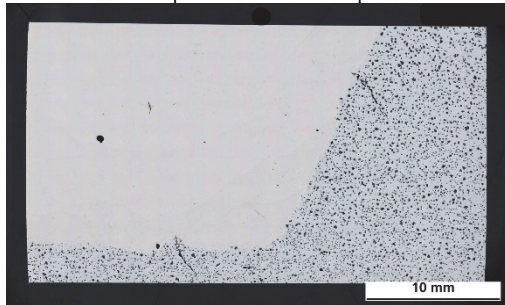
Hardness map at the edge of the fusion zone



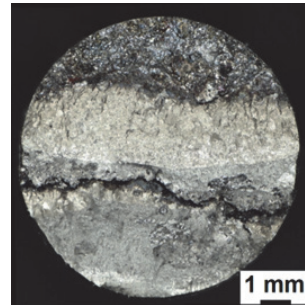
SEM picture of a small pore



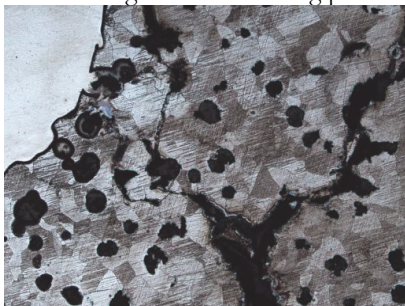
Solidification structure inside the fusion zone



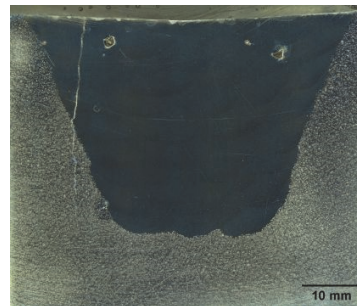
Etched section of the cross section of a bending specimen with small pores and a crack in the welding filler coming from the welding process



Fracture surface of an axial specimen with failure in the interface between welding filler and base material



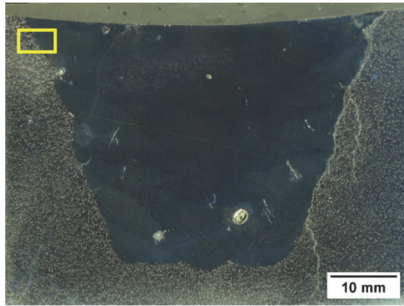
Etched section of the fusion line and the heat affected zone with hard martensitic and ledeburitic microstructures



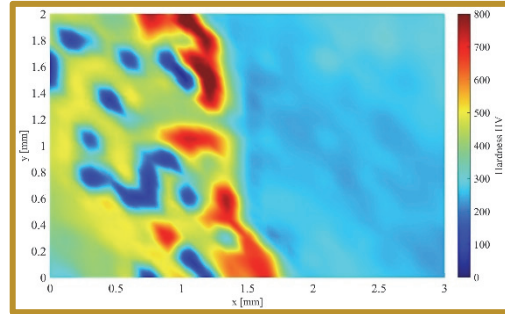
Macroscopic picture of the etched welding with the crack propagating from the surface through the welding filler and the base material

Table 7: Examples of micrographs, hardness maps and etched sections for EN-GJS-450-18 with welds.

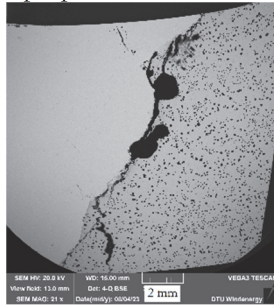
EN-GJS-700-2 cast block



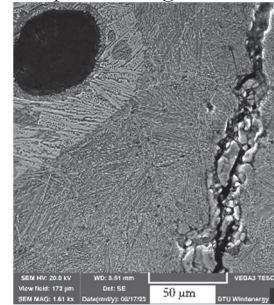
Macroscopic picture of the etched welding



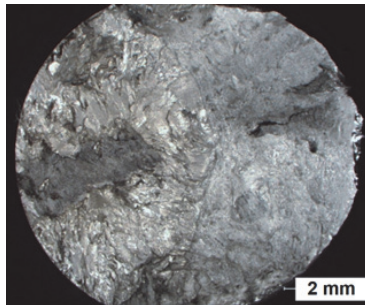
Hardness map at the edge of the fusion zone



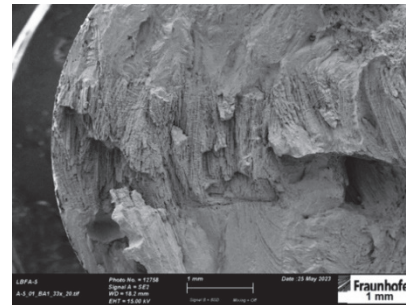
Crack initiation and propagation along the fusion zone and the heat affected zone



Crack propagation through the martensite



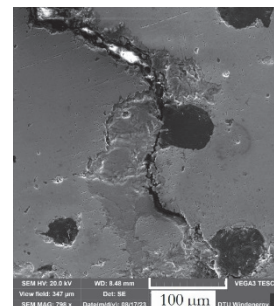
Fracture surface of an axial specimen with failure in the welding filler



Fracture surface of an axial specimen with failure in the welding filler; over a wide area delamination in the welding filler is present



Etched section of the fusion line and the heat affected zone with hard martensitic and ledeburitic microstructures



Crack propagating along segregations and graphite nodules

Table 9: Examples of micrographs, hardness maps and etched sections for EN-GJS-700-2 with welds.



CONCLUSIONS

During the conducted investigations, it was found that all investigated materials showed a high loss in fatigue strength for the welded condition in comparison to the base material. While the welding procedure with hand-held electrodes could be conducted easily for EN-GJS-400-18LT and EN-GJS-700-2, welding of the high silicon EN GJS 450-18 showed microcracks in the fusion line and the lowest fatigue strength. In consequence, using the solid solution strengthened material to perform a lightweight design will deliver a negative effect, when welding might be necessary to prevent rejects.

The derived fatigue data are now useful for a comparison of the local stresses and the cyclic strain behavior under load to decide whether or not a repair welding of a wind energy component is applicable or not. Nevertheless, it can be stated that the fatigue strength, especially under tensile loading, might be too low for most of the typical thick-walled machinery components in wind energy application. Especially in highly loaded areas and stress hotspots, local stresses might exceed 100 MPa stress amplitude. This becomes more crucial when wind energy components are optimized in the direction of lightweight.

The investigations and results presented provide an impression of the cyclic load-bearing capacity of welded, thick-walled cast iron with nodular graphite. Realistic welding boundary conditions were deliberately used to ensure applicability in almost any environment. The tests show that a significant reduction in fatigue strength is to be expected for each base material, which reaches values of up to 75 % under tensile swelling and alternating loads, particularly in the case of EN-GJS-450-18. Unfortunately, this material showed many local, small cracks in the transition area and, with the selected welding edge conditions, was not very suitable for welding. For EN-GJS-400-18LT and EN-GJS-700-2, the cyclic load capacity under pure axial load is still 65 % or more with welds present. In the case of superimposed stress gradients, as in the case of the bending specimens, however, a reduction in the load-bearing capacity of 60 % can also be expected for the ferritic EN-GJS-400-18LT. Depending on the application and load, the characteristic values determined here can be used to decide whether welding for repair purposes is feasible and whether the required minimum strength can be achieved.

ACKNOWLEDGEMENTS

The results presented in this paper were derived during the research project “nodularWELD³” (Schoenborn, 2017), grant number 0324273A. For the funding of this project, sincere thanks are given to the German Federal Ministry for Economic Affairs and Climate Action (BMKW). Furthermore, all project partners are thanked for their participation and support to complete this project successfully.

NOMENCLATURE

b [-]	fatigue strength exponent
c [-]	fatigue ductility exponent
d [mm]	diameter of the specimen
E [GPa]	Young’s modulus
f [Hz]	test frequency
k [-]	slope of the SN curve in the medium cycle fatigue range
k^* [-]	slope of the SN curve after the knee point
K' [MPa]	cyclic hardening coefficient
K_t [-]	stress concentration factor
M [-]	mean stress sensitivity
N [-]	number of cycles
n' [-]	cyclic hardening exponent
N_f [-]	number of cycles to failure
N_i [-]	number of cycles to crack initiation
N_k [-]	number of cycles at the knee point
N_{lim} [-]	limit number of cycles
P_s [%]	probability of survival



$R'_{p0,2}$ [MPa]	cyclic yield strength
R_e, R_σ [-]	load ratio under constant amplitude loading for strain and stress
T_σ [-]	scatter band
$\varepsilon_{a,e}$ [%]	elastic strain
$\varepsilon_{a,p}$ [%]	plastic strain
$\varepsilon_{a,t}$ [%]	total strain under constant amplitude loading
ε_f [m/m]	fatigue ductility coefficient
$\sigma_{a,n,k}$ [MPa]	nominal stress amplitude at the knee point
$\sigma_{a,n,Nlim}$ [MPa]	Nominal stress amplitude at the limit number of cycles

REFERENCES

- [1] DIN EN 1563 (2019). Founding – Spheroidal graphite cast irons, Normenausschuss Gießereiwesen (GINA) im DIN Deutsches Institut für Normung e.V.: DIN EN 1563:2018.: Deutsche Fassung EN 1563:2019-04, ICS 77.080.10, Beuth publishing DIN, Berlin, DOI: 10.31030/2792445
- [2] DNV (2016). Machinery for wind turbines, DNVGL-ST-0361, DNV AS.
- [3] Schoenborn, S. (2023). NodularWELD – Identification and optimisation of welding parameters for repair welding of cast iron components with nodular graphite with adjustment of a defined microstructure to ensure comparable static and cyclic strength characteristics of the weld zone, heat-affected zone and base material, final report, BMWK, Darmstadt, grant number 0324273A, Fraunhofer LBF.
- [4] Bleicher, C., Schoenborn, S. and Kaufmann, H. (2022). Cyclic material behavior of repair welded thick-walled nodular cast iron for wind energy application, Proceedings of the International Offshore and Polar Engineering Conference, 32nd International Ocean and Polar Engineering Conference, ISOPE, Shanghai, pp. 2984 – 2989
- [5] Bleicher, C., Schoenborn, S. and Kaufmann, H. (2023). A comparison of the fatigue strength of repair welded nodular cast iron materials for thick-walled applications, Proceedings of the International Offshore and Polar Engineering Conference, 33rd International Ocean and Polar Engineering Conference, ISOPE, , pp. 3098 – 3105.
- [6] Bleicher, C, Schoenborn, S, Kaufmann, H., A comparison of the fatigue strength of repair welded nodular cast iron materials for usage in wind energy components, International Journal of Offshore and Polar Engineering, accepted for publication, 2024.
- [7] Bleicher, C., Schoenborn, S. and Kaufmann, H. (2023). An investigation on the fatigue strength of repair welded nodular cast iron for heavy sections, Procedia Structural Integrity, 47, p. 478-487, DOI: 10.1016/j.prostr.2023.07.076.
- [8] DVS – German Welding Society, (2004). Bruchmechanische Bewertung von Fehlern in Schweißverbindungen Merkblatt DVS 2401, DVS technical books, 101.
- [9] Baer, W., (1996). Bruchmechanische Bewertung ferritischer Gusseisenwerkstoffe sowie artgleicher Schweißverbindungen bei statischer Beanspruchung. TU Bergakademie Freiberg, dissertation.
- [10] VDMA Guideline, (2013). 23902:2014-07 - Leitlinie für den bruchmechanischen Nachweis von Planetenträgern aus EN-GJS-700-2 für Getriebe von Windenergieanlagen. Verband Deutscher Maschinen- und Anlagenbau e.V. (VDMA), Mechanical and Plant Engineering.
- [11] International Nickel, (1969). Schweißen von Sphäroguss, 1th edition, Germany, Düsseldorf.
- [12] Schock, D. (1982). Elektrisches Kaltschweißen von Gusseisen mit Kugelgraphit mit Stahlelektroden, Giesserei, 69(5), pp. 125 – 127.
- [13] Schramm, A. (1997). Schweißen von Gusseisen – Qualitätsdatenbank, Kontruieren + giessen, 2(4), pp. 9 – 14.
- [14] Holdstock, R. and Alizadehshamsabadi, M. (2023). Repair welding of spheroidal graphite cast iron, Proceedings of the 2nd Congress for Intelligent Combining of Design, Casting, Computer Simulation, Checking and Cyclic Behaviour for Efficient Cast Components, Ceight Casting 2023, Darmstadt, Germany, p. 59 – 66.
- [15] EN ISO 4063 (2011). Welding and allied processes - Nomenclature of processes and reference numbers (ISO 4063:2009, Corrected version 2010-03-01); Trilingual version EN ISO 4063:2010, Beuth publishing DIN, DOI: 10.31030/1736984.
- [16] Schuetz, W. (1967). Über eine Beziehung zwischen der Lebensdauer bei konstanter und veränderlicher Beanspruchungsamplitude und ihre Anwendbarkeit auf die Bemessung von Flugzeugbauteilen. Dissertation, Technische Hochschule München, 1965 und Zeitung für Flugwissenschaften, 15(11), pp. 407 – 419.
- [17] SEP1240 (2006). Prüf- und Dokumentationsrichtlinie für die experimentelle Ermittlung mechanischer Kennwerte von Feinblechen aus Stahl für die CAE-Berechnung, 1. issue, STAHL-EISEN-Prüfblätter, Stahlinstitut VDEh.



- [18] Ramberg, W. and Osgood, W. R. (1943) Description of stress–strain curves by three parameters. NACA Techn. Rep. 902, NACA.
- [19] Coffin, L. A. (1954). A study of the effects of cyclic thermal stresses on a ductile metal. *Trans. ASME*, 76, pp. 931 – 950.
- [20] Manson, S. S. (1965). Fatigue: A complex subject – some simple approximations. *Experimental Mechanics*, 5(7), pp. 45 – 87.
- [21] Basquin, O. H. (1910). The exponential law of endurance tests. *American Society Test, Materials Proceedings*, No. 10, pp. 625 – 630.
- [22] Morrow, J. D. (1965). Cyclic plastic strain energy and fatigue of metals, ASTM STP 378, American Society for Testing and Materials, pp. 45 – 87.
- [23] Nieslony, A., el Dsoki, C., Kaufmann, H. and Krug, P. (2008). New method for evaluation of the Manson-Coffin-Basquin and Ramberg-Osgood equations with respect to compatibility, *International Journal of Fatigue*, 30, pp. 1967 – 1977, DOI: 10.1016/j.ijfatigue.2008.01.012.
- [24] Spindel, J. E. and Haibach, E. (1979). The method of maximum likelihood applied to the statistical analysis of fatigue data including run-outs, S.E.E. International Conference, University of Warwick, Coventry, pp. 7.1 – 7.23, DOI: 10.1016/0142-1123(79)90012-4.
- [25] Stoerzel, K. and Baumgartner, J. (2021). Statistical evaluation of fatigue tests using maximum likelihood, in *Materials Testing, De Gruyter*, 63(8), pp. 714 – 720, DOI: 10.1515/mt-2020-0116.
- [26] Sonsino, C. M., (2007). Course of SN-curves especially in the high-cycle fatigue regime with regard to component design and safety, in *International Journal of Fatigue*, 29, pp. 2246 – 2258, DOI: 10.1016/j.ijfatigue.2006.11.015.
- [27] Bleicher, C, Wagener, R, Kaufmann, H, and Melz, T (2015). Fatigue strength of nodular cast iron with regard to heavy-wall application, *Materials Testing, Carl Hanser Verlag*, 9, pp. 723 – 731, DOI: 10.3139/120.110782.
- [28] Bleicher, C., Wagener, R., Kaufmann, H. and Melz, T. (2017). Fatigue Assessment of Nodular Cast Iron with Material Imperfections. *SAE International Journal of Engines*, 10 (2), pp. 340-349, DOI: 10.4271/2017-01-0344.
- [29] Schoenborn, S. (2020). SWL Eisenguss – Ableitung von synthetischen Wöhlerlinien für Eisengusswerkstoffe, Final report, IGF project 16257 BG, FVG.
- [30] Niewiadomski, J., Bleicher, C. and Kaufmann, H. (2021). Influence of the Chill Casting Process on the Cyclic Material Behavior of Nodular Cast Iron, 31th International Ocean and Polar Engineering Conference – Rodos, Greece, Online/Virtual Conference, Proceedings, pp. 2404 – 2411.
- [31] Forschungskuratorium Maschinenbau (FKM), (2020). FKM-Richtlinie – Rechnerischer Festigkeitsnachweis für Maschinenbauteile aus Stahl, Eisenguss- und Aluminiumwerkstoffen, 7, revised issue, Frankfurt am Main.
- [32] DIN 945, (2019). Microstructure of cast irons - Part 1: Graphite classification by visual analysis (ISO 945-1:2019); German version EN ISO 945-1:2019., Beuth publishing DIN, Berlin, DOI: 10.31030/3091837.